

RESEARCH ARTICLE

Wake structures behind a swimming robotic lamprey with a passively flexible tail

Megan C. Leftwich^{1,*}, Eric D. Tytell^{2,†}, Avis H. Cohen³ and Alexander J. Smits⁴

¹Neutron Science and Technology Group, Physics Division, Los Alamos National Laboratory, Los Alamos, NM 87545, USA,

²Department of Mechanical Engineering, Johns Hopkins University, Baltimore, MD 21218, USA, ³Department of Biology, University of Maryland, College Park, MD 20742, USA and ⁴Department on Mechanical and Aerospace Engineering, Princeton University, Princeton, NJ 28544, USA

*Author for correspondence at present address: Department of Mechanical and Aerospace Engineering, The George Washington University, Washington, DC 20052, USA (mleftwich@gwu.edu)

†Present address: Department of Biology, Tufts University, Medford, MA 02155, USA

Accepted 12 October 2011

SUMMARY

A robotic lamprey, based on the silver lamprey, *Ichthyomyzon unicuspis*, was used to investigate the influence of passive tail flexibility on the wake structure and thrust production during anguilliform swimming. A programmable microcomputer actuated 11 servomotors that produce a traveling wave along the length of the lamprey body. The waveform was based on kinematic studies of living lamprey, and the shape of the tail was taken from a computer tomography scan of the silver lamprey. The tail was constructed of flexible PVC gel, and nylon inserts were used to change its degree of flexibility. Particle image velocimetry measurements using three different levels of passive flexibility show that the large-scale structure of the wake is dominated by the formation of two pairs of vortices per shedding cycle, as seen in the case of a tail that flexed actively according to a pre-defined kinematic pattern, and did not bend in response to fluid forces. When the tail is passively flexible, however, the large structures are composed of a number of smaller vortices, and the wake loses coherence as the degree of flexibility increases. Momentum balance calculations indicate that, at a given tailbeat frequency, increasing the tail flexibility yields less net force, but changing the cycle frequency to match the resonant frequency of the tail increases the force production.

Key words: flexibility, thrust production, anguilliform swimming, hydrodynamics, lamprey.

INTRODUCTION

The swimming motions of fishes are the result of an intricate balance of forces. The axial musculature produces forces that bend the body, which has elastic properties that may resist or aid the muscular forces. The body motion then moves the fluid around the animal, producing forces back on the body. The swimming motion we observe comes from a balance between the internal muscle and body forces and the external fluid forces (Gray, 1933; Jordan, 1996).

In particular, the stiffness of the body may be important for effective swimming. Recently, Tytell et al. (Tytell et al., 2010) examined the coupling between the body of an anguilliform swimmer and the fluid in a computational model, and found different optimal body stiffnesses for high-speed swimming, high accelerations and low-power consumption. Similarly, McHenry et al. (McHenry et al., 1995) found that changes in body stiffness could alter both body wavelength and wave speed in rubber models of fish. Other work suggests that fishes can actively control the stiffness of the body; properly timed muscle activation could increase body stiffness by up to a factor of seven (Long, 1998).

Passive stiffness may have a particularly strong effect near the tip of the tail. Analytical, experimental and robotic approaches indicate that the bulk of the thrust force is produced at the tip of the tail (Lighthill, 1971; Leftwich and Smits, 2011; DuBois and Ogilvy, 1978). The fin rays that make up the caudal fin are actively controlled (Flammang and Lauder, 2008). Nevertheless, the bulk of the axial musculature is located more anteriorly, so the force that the caudal fin can produce to resist fluid forces may be relatively

small. Therefore, passive interactions between the fluid and the fin are considered important.

We investigated the role of tail flexibility in anguilliform swimming using the robotic lamprey described by Hultmark et al. (Hultmark et al., 2007) and Leftwich and Smits (Leftwich and Smits, 2011). The stiff, actively controlled tail used in these earlier studies was replaced by a passively flexible tail with a morphology modeled on computer tomography (CT) scans of the silver lamprey. The tail was constructed of flexible PVC gel, and nylon inserts were used to change its degree of flexibility.

Body flexibility is likely to be particularly important for anguilliform swimmers, which is the reason we designed the robot to mimic this mode of swimming. In general, anguilliform swimmers are more flexible than other fishes (Aleyev, 1977). Similarly, body curvature tends to be higher for anguilliform swimming (Aleyev, 1977; Gillis, 1998). Thrust production of flexible bodies was considered numerically in two recent papers: Masoud and Alexeev found that at low Reynolds numbers, oscillating flexible wings at resonance greatly enhanced the thrust production (Masoud and Alexeev, 2010), and Ferreira de Sousa and Allen (Ferreira de Sousa and Allen, 2011) investigated flexible membranes of flapping wings over the time of a flapping cycle.

The anguilliform mode of swimming also has several distinct hydrodynamic features. Anguilliform swimmers tend to produce a wake with two separate vortex rings per full tailbeat (Müller et al., 2001; Tytell and Lauder, 2004), referred to as a 2P wake in the terminology of Williamson and Roshko (Williamson and Roshko, 1988). In contrast, most carangiform swimmers produce a single



Fig. 1. Robotic lamprey tail used in the present study. The entire robot is shown without the foam padding, waterproof latex skin and flexible tail.

vortex ring per cycle that links up with the one from the previous cycle (e.g. Nauen and Lauder, 2002), called a 2S wake. Recent computational work indicates that the 2P wake structure is related to the Strouhal number, which can be calculated as $St = \omega_f A / U_\infty$, where ω_f and A are the tailbeat frequency and amplitude, respectively, and U_∞ is the swimming speed (Borazjani and Sotiropoulos, 2008). Strouhal number, in turn, can be altered by changing body stiffness (Tytell et al., 2010).

Here, we examine the importance of passive flexibility in the tail of a robotic lamprey. Passive flexibility in swimming has been investigated computationally by Zhu and Shoele (Zhu and Shoele, 2008) and Shoele and Zhu (Shoele and Zhu, 2009), and experimentally by Tangorra et al. (Tangorra et al., 2010). These studies, like the present study, investigated the connections between force, wake structure and flexibility. In this study, we used three different degrees of tail flexibility and the resulting swimming speeds, wake structures and momentum estimations are reported. In addition, we investigated the role of resonance in the wake structure for a given flexibility.

MATERIALS AND METHODS

Experimental setup

The experiments were carried out in the wake of a robotic swimming lamprey. The robot was adapted from that used by Hultmark et al. (Hultmark et al., 2007) and Leftwich and Smits (Leftwich and Smits, 2011) by replacing the original stiff tail with a custom-made flexible tail. Fig. 1 shows the entire robot with the padding, waterproof skin and tail removed. The tail was attached to the robot by inserting the last two motors into the anterior third of the molded tail. To keep the overall length of the robot constant, the total number of servo motors was reduced from 13 to 11. The servo motors were controlled by a BasicX Stamp microcontroller (Parallax, Inc., Rocklin, CA, USA) to create the anguilliform swimming motion of the lamprey. Reducing the number of motors had an almost negligible effect on the resulting waveform of the lamprey body posterior to the flexible tail. Three different degrees of tail flexibility were tested. The robot was mounted in a recirculating water channel (Fig. 2). This apparatus is well characterized and has a 3% variation of the mean velocity at higher velocities (0.285 m s^{-1}) (Buchholz, 2006). Further details of the robot construction, operation and kinematics can be found in Hultmark et al. (Hultmark et al., 2007) and Leftwich and Smits (Leftwich and Smits, 2011).

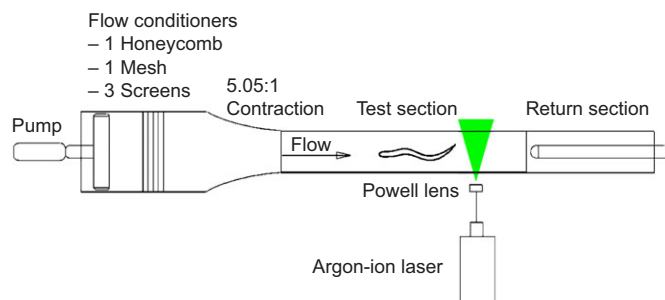


Fig. 2. Sketch of the water channel showing the laser sheet and camera arrangements from the top.

The Reynolds number [$Re = LU_\infty/\nu$, based on body length (L) = 0.9 m, $U_\infty = 0.1 \text{ m s}^{-1}$ and the kinematic viscosity of the fluid (ν) = 1.00×10^{-6}] was approximately 85,000 (this varied slightly as the flow speed was tuned to hold Strouhal number constant), and the Strouhal number (St) was 0.55. For each of the flexible tails, the flow speed was tuned to reach a Strouhal number of 0.55. The incoming flow speed, i.e. swimming speed (U_∞), was adjusted to compensate for any changes in amplitude (A) due to flexibility. For all but the resonant frequency experiment, the frequency was constant at 0.56 Hz. This Strouhal number is higher than that of the silver lamprey in steady swimming, which is close to 0.35 (Hultmark et al., 2007).

When determining the swimming speed of the robot with the various flexible tails, the Strouhal number was not set *a priori*. An air-bearing carriage allowed the robot to move freely in the streamwise direction. The robot was powered on and began to swim upstream. The incoming flow speed was then adjusted until the robot was able to hold its station. This speed was considered the ‘free swimming speed’.

The velocity field in the half wake behind the swimming robot was measured using particle image velocimetry (PIV). In these experiments, the flow was seeded with silver coated hollow ceramic spheres with a diameter of $100 \mu\text{m}$ and an average specific gravity of 1.01 (Conduct-O-Fil AGSL-150-30 TRD, Potters Industries Inc., Valley Forge, PA, USA). The particles were illuminated by a Spectra Physics 2020 argon-ion laser with a wavelength of 488 nm (Newport Corporation, Mountain View, CA, USA). The laser was then used to create a light sheet with an optical fiber delivery system and a Powell lens (Oz Optics Ltd, Ottawa, ON, Canada). The sheet thickness was typically 1.5 mm. The sheet was oriented parallel to the robot in the plane in which the robot was swimming. A Redlake MotionXtra HG-LE camera (Redlake, IDT, Tallahassee, FL, USA) was used to capture the images. A Stanford Research Systems DG535 Digital Delay/Pulse Generator (Stanford Research Systems, Inc., Sunnyvale, CA, USA) was used to control the camera timing. Image pairs were captured with a time delay of 11 ms between images. Ten image pairs were captured each second, with typical exposure times of 3 ms. The camera was mounted above the water channel at a 90 deg angle to the laser sheet. The experimental configuration for PIV is shown in Fig. 2. The results presented here represent instantaneous velocity and vorticity contours.

Flexible tail construction

The tail was made using a moldable PVC polymer (M-F Manufacturing, Fort Worth, TX, USA). The shape of the tail was modeled on CT scan data of a 29 cm silver lamprey, *Ichthyomyzon unicuspis*, provided by Dr Frank Fish (personal communication),



Fig. 3. Flexible tail. Nylon insert (orange) is visible on the right. The last two servo motors are inserted into the hollow part on the left.

which consisted of data slices taken every 2 mm. ImageJ software (National Institutes of Health, Bethesda, MD, USA) allowed us to extract the body points from each slice. The mold was scaled using the coordinates of the posterior third of the animal. The anterior third of the mold was hollow, to allow insertion of the last two motors, so that this part was active. The remaining part of the tail was passive, and a thin nylon insert of constant planform but different thicknesses was used to control the degree of flexibility (the insert is seen in orange in Fig. 3). The length of the flexible part of the tail, l_{pass} , corresponded to approximately 20% of the total length of the robot.

Three tails of different flexibility were constructed. The degree of tail flexibility was characterized by determining its passive deformation. Fig. 4 depicts the passive deformation experiment. With the tail attached to the robot, the robot was clamped rigidly at the point where the tail became passively flexible. The tail was mounted horizontally and allowed to deform under its own weight (Fig. 5). The distance from the tip of the deformed tail (illustrated by solid lines in Fig. 4) to the centerline of the undeformed tail (illustrated by dashed lines in Fig. 4) was labeled y_{def} . Hence we define the non-dimensional flexibility parameter, F , as:

$$F = \frac{y_{\text{def}}}{l_{\text{pass}}} \quad (1)$$

For reference, the flexural stiffness (EI) was also estimated according to:

$$EI = \frac{mgl_{\text{pass}}}{3y_{\text{def}}} \quad (2)$$

where m is the mass of the tail (Den Hartog, 1961) and g is acceleration due to gravity. Eqn 2 is valid for small deflections and constant cross-section, whereas y_{def} is large and the cross-section varies with distance along the tail, so we provide the estimates for reference only. Note that Long (Long, 1998) reports values of EI for eels that range between 1 and $2 \times 10^{-4} \text{ Nm}^2$ for passive eel bodies.

To quantify the relative coherence of the various wakes, we also calculated the average turbulence intensity, I , over a cycle of motion for each case. This is defined as $I = \mathbf{u}'/U$, where \mathbf{u}' is the variance of the turbulent velocity fluctuations [$\mathbf{u}' = \sqrt{1/2(u'^2 + v'^2)}$, where u' and v' are the fluctuations of the streamwise and spanwise velocity, respectively] and U is the Reynolds-averaged mean velocity ($U = \sqrt{U^2 + V^2}$, where U and V are the mean components of the streamwise and spanwise velocity, respectively).

To investigate the role of material resonance, the frequency response of tail 2 was examined by actuating it over a range of frequencies from 0.1 to 0.65 Hz while submerged in quiescent water.

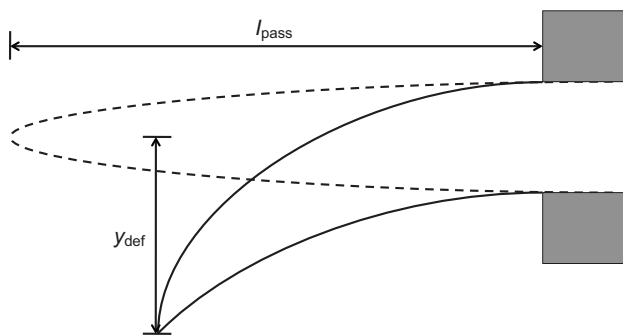


Fig. 4. Experimental setup used to determine the flexibility parameter, F , of the flexible tails. l_{pass} , length of the flexible part of the tail; y_{def} , distance from the tip of the deformed tail to the centerline of the undeformed tail.

The tail motion was filmed, and from the video images, the peak-to-peak amplitude of the tip of the tail was measured. The results are shown in Fig. 6. A resonant plateau is found in the range of frequencies from 0.22 to 0.34 Hz. The center of this plateau was chosen as the resonant frequency for this tail, indicated by the vertical line in the figure. Experiments with this tail were performed at the resonant frequency (0.28 Hz) and at twice the resonant frequency (0.56 Hz). The Strouhal number was kept constant for these two cases by reducing the swimming speed appropriately. It is not expected that the incoming flow will greatly affect the resonant frequency given the broad resonant curve and large plateau seen in Fig. 6.



Fig. 5. The three flexible tails – (A) tail 1, (B) tail 2 and (C) tail 3 – deflecting under their own weight.

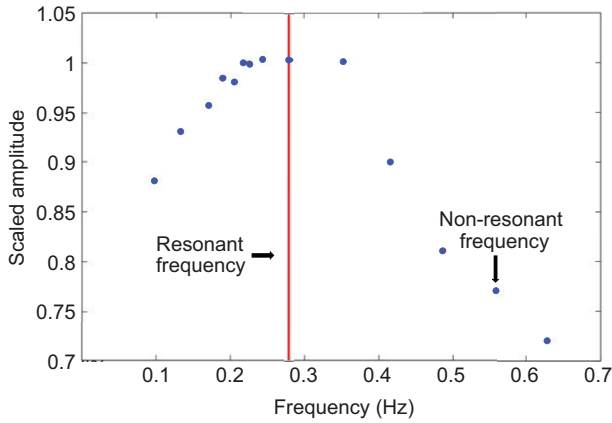


Fig. 6. Forced oscillation response of tail 2. The resonant frequency was chosen as the center of the resonant plateau, 0.28 Hz.

Force calculations

The net force produced by the lamprey was estimated from the velocity fields (obtained from PIV experiments) using a two-dimensional control volume analysis. This analysis is a standard application of the momentum equation. Details of the control volume method and all equations used here can be found in most fluid

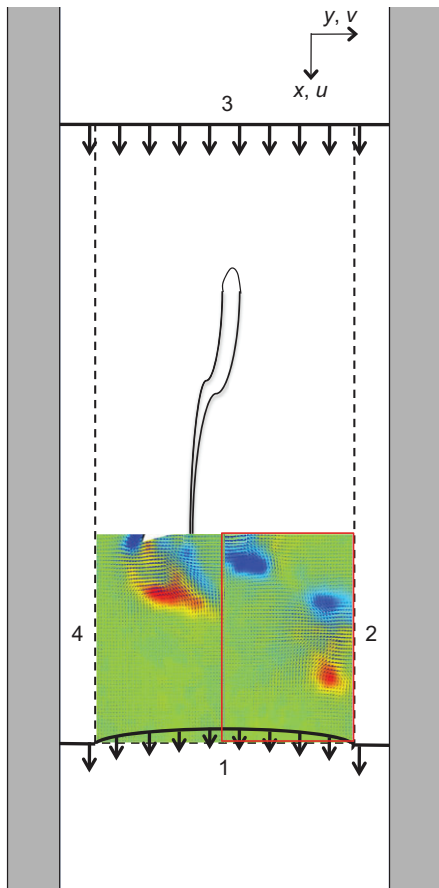


Fig. 7. Schematic of control volume (dashed lines) for momentum calculations. Colors indicate vorticity. The right half of the wake (indicated by the red box) was not measured directly, but is rather a mirrored and phase-shifted version of the left half, assuming that the wake is left-right symmetrical. The numbers 1 to 4 correspond to the terms in Eqn 4.

dynamics textbooks (e.g. Smits, 2000). The control volume contained the entire robot, as shown in Fig. 7. The incoming velocity is known for each experiment, and was assumed to be uniform across the inflow area. The PIV data was obtained only over the left side of the wake, so the full wake was constructed by mirroring the data and offsetting it in time by half a cycle. The portion of the control volume along the robot is neglected as reliable data is not available.

To calculate the net force, we used the integral form of the momentum equation:

$$\mathbf{F} = \frac{\partial}{\partial t} \int \rho \mathbf{V} dV + \int (\mathbf{n} \cdot \rho \mathbf{V}) \mathbf{V} dA. \quad (3)$$

Here, \mathbf{F} is the force acting on the fluid, t is time, ρ is the fluid density, \mathbf{V} is the fluid velocity and \mathbf{n} is the unit normal vector at the boundary of the control volume. We neglect the contributions to the momentum flux through the sides of the control volume upstream of the tail, for which there are no PIV data, and the thrust due to pressure differences. In other words, \mathbf{F} is the force due to the momentum flux out of the control volume and the rate of change of momentum inside the control volume.

To determine the rate of change of momentum, the momentum contained within the control volume at each phase was computed and a central difference scheme in time was used to determine the rate of change of momentum between phase intervals. Thus:

$$T(t) = \sum_1 \rho u^2 \Delta L_y + \sum_2 \rho uv \Delta L_x - \sum_3 \rho u^2 \Delta L_y - \sum_4 \rho uv \Delta L_x + \frac{1}{2\Delta t} \left[\left(\sum_x \sum_y \rho u \Delta L_y \Delta L_x \right)_{i+1} - \left(\sum_x \sum_y \rho u \Delta L_y \Delta L_x \right)_{i-1} \right], \quad (4)$$

where T is the force component acting on the body in the streamwise direction. The terms numbered 1 to 4 correspond to the surfaces shown in Fig. 7 and represent the streamwise momentum flux through each of those surfaces. The variables u and v are the streamwise and spanwise velocity components, respectively, and ΔL_x and ΔL_y are the corresponding discrete length elements in the x and y directions, respectively. As the PIV data are discrete, a summation of the known velocities is used to approximate the integral. The time-averaged net force \bar{T} can be found by calculating the force at each phase and then averaging over the entire cycle.

In addition to the measurements of T , the motion of each tail was digitized and the thrust (P) and lateral force (Q) for each tail were estimated using large-amplitude elongated body theory (Lighthill, 1971), as follows:

$$(P, Q) = \left[m(s)w \left(\frac{\partial y}{\partial t}, \frac{\partial x}{\partial t} \right) - \frac{1}{2} m(s)w^2 \left(\frac{\partial x}{\partial s}, -\frac{\partial y}{\partial s} \right) \right]_{s=L}^{\text{minimize}} - \frac{d}{dt} \int_0^L m(s) \left(\frac{\partial y}{\partial s}, \frac{\partial x}{\partial s} \right) ds, \quad (5)$$

where x and y are the coordinates of the midline, s is the arc length along the midline from head ($s=0$) to tail ($s=L$), $m(s)$ is the mass per unit length and w is the velocity perpendicular to the midline, where:

$$w = \frac{\partial y}{\partial t} \frac{\partial x}{\partial s} - \frac{\partial x}{\partial t} \frac{\partial y}{\partial s}. \quad (6)$$

Note that the x position includes the swimming speed U , so that $x = -Ut + x'$, where x' is the motion relative to the center of mass.

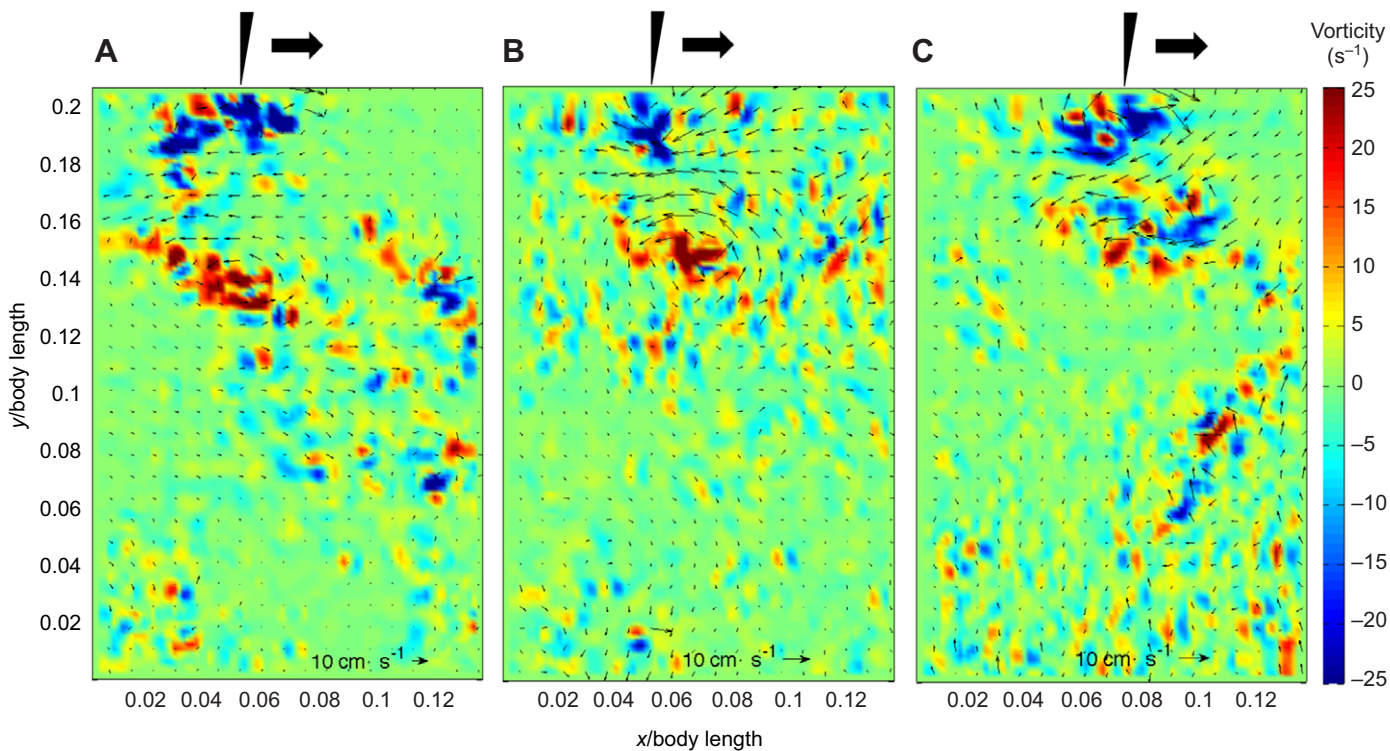


Fig. 8. The half wake behind the swimming lamprey robot fitted with (A) tail 1 (least flexible), (B) tail 2 and (C) tail 3 (most flexible). The robot is out of view above the image. Flow is from top to bottom. Instantaneous vorticity contours are plotted in color, and all figure have the same contour levels. Arrows indicate the magnitude and direction of flow with the mean values subtracted. The position of the tail is indicated by at the top of each image, and the arrow indicates the direction of tail motion.

Also, note that $\partial x/\partial s = \cos\theta$, where θ is the angle of the tail. For high thrust, therefore, one should minimize the second term in Eqn 5, which is achieved if $\cos\theta$ is small when w^2 is large (i.e. tail angle is approximately 45 deg just before the tail crosses the midline) (Lighthill, 1970).

RESULTS
Wake structure

Table 1 shows the characteristics of the flexible tails. Tail 1 is the least flexible tail, with a flexural stiffness (EI) of 1.9 Nm^2 , corresponding to an average Young’s modulus (E) of 0.23 MPa . The most flexible tail, tail 3, is extremely flexible and deforms almost completely under its own weight. The damped natural frequency (in air) decreases by 12% from tail 1 to tail 2, and by 35% from tail 1 to tail 3. The damping coefficient decreases by 58% from tail 1 to tail 2 and by 96% from tail 1 to tail 3 (see Table 1); in other words, oscillations persist much longer in tail 3 than in tail 1.

The disorganized vortex structure in the wakes of the flexible tails is seen clearly by direct visualization of the flow patterns, as shown in Fig. 8. At this Strouhal number (0.55), all three tails produce two pairs of vortical regions per tailbeat, but the vorticity becomes more disorganized as tail flexibility increases. In Fig. 8A

(tail 1), the pair of vortices from the most recent half cycle is visible at the top of the image, near the center. The red vortex is the secondary vortex from the previous cycle, and the blue vortex is the starting–stopping vortex from the most recent change in tail direction – it will separate into two vortices. The pair is aligned in the flow direction and induces a velocity between them in the perpendicular direction. The wake behind the lamprey robot fitted with an actively flexing tail is shown in Fig. 9 for comparison. In this case, the pair of vortices is much more distinct. In the flexible case, however, the larger vortices are composed of several small vortices of the same sign. They convect together downstream for a short distance, and then begin to break up.

The wake produced by tail 2 (Fig. 8B) is similar to that of tail 1 (Fig. 8A). Again, the pair of vortices on the visible half of the wake is in the upper center of the image. The red vortex represents the secondary vortex from the previous stopping–starting motion, and the blue vortex is the primary vortex from this half cycle. The main vortex cores, however, are smaller than those in the wake of tail 1, and are composed of several vortex structures with the same sign. These small vortices convect downstream, but do not retain coherence for as long as with the stiffer tail.

The most flexible tail, tail 3, has the least coherent wake structure (Fig. 8C). The oppositely signed vortex pair for this half cycle is visible at the top of Fig. 8C. In this case, the areas of positive and negative vorticity are not as distinct as they are in the wakes of tails 1 and 2. The vortex structures, smaller and more numerous, loosely form a pair of vortices. However, the lack of organization and mixture of positive and negative vorticity in each member of the pair causes the overall structure to break down very quickly. Instead of convecting downstream as a cohesive element, only these small vortices are present in the wake. Their similar strengths and uniform

Table 1. Characteristics of the flexible robotic tails used in the present study

Tail	Insert thickness (mm)	Flexibility factor (F)	Flexural stiffness (EI ; $\times 10^{-4}\text{ Nm}^2$)
1	2.4	0.47	1.9
2	1.6	0.63	1.4
3	0.8	0.95	1

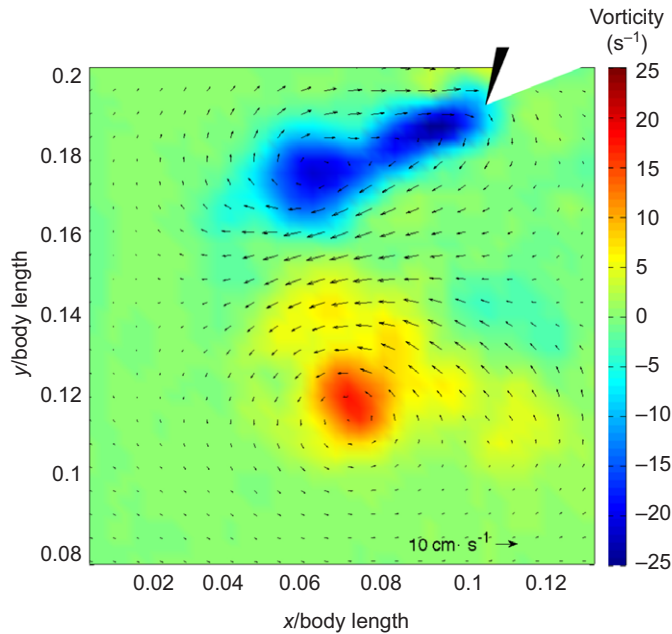


Fig. 9. Phase-averaged wake of the robotic lamprey with an actively flexing tail. After Hultmark et al. (Hultmark et al., 2007).

distribution work to cancel each other out quickly. Hence, the overall strength of the circulation decreases at high flexibility.

For comparison, previous data from the same robot with the actively flexing tail are shown (Fig. 9) [after Hultmark et al. (Hultmark et al., 2007)]. Unlike in the present study, the tail flexes substantially but actively, and does not deform appreciably in response to fluid forces. Nevertheless, the wake is similar to those from passively flexible tails (shown in Fig. 8), with two pairs of vortices shed per cycle, but the vortices are substantially more coherent.

In addition to imaging the wake structures at a constant Strouhal number, an air-bearing carriage above the water channel was used to determine the free swimming speed of the lamprey robot with each flexible tail. Previous work (Hultmark et al., 2007) determined this for the robot with the stiff, active tail. From this data, the steady swimming speed and Strouhal number were determined for each tail (Fig. 10). Fig. 10A shows the swimming speeds (m s^{-1}) of the robot with each tail. We see that the active tail produces the fastest swimming whereas the most flexible tail is the slowest (discounting tail 2 at resonance, which is operating at half the frequency; see Resonance frequency below). From the active tail to tail 1, there is a 11% decrease in swimming speed; the swimming speed of tail 2 decrease a further 17% from tail 1, and that of tail 3 decreases from tail 2 by 29%.

Swimming speeds were used to calculate the steady-swimming Strouhal numbers of the tails. The results, given in Fig. 10B, show an increase in Strouhal number from the active tail to tail 1 and a continued increase to tail 2 (indicating decreased performance). Tail 3, however, shows a slightly lower Strouhal number than tail 2 (3.4%), primarily because of a decrease in tip-to-tip amplitude.

Axial force production

To compare the force production of the flexible tails, the axial force (i.e. the force in the swimming direction) for an entire cycle was estimated using Eqn 4, and then summed over an entire cycle. Fig. 11 shows the outward momentum flux for the three flexible tails. These are the average values for 20 cycles of each tail.

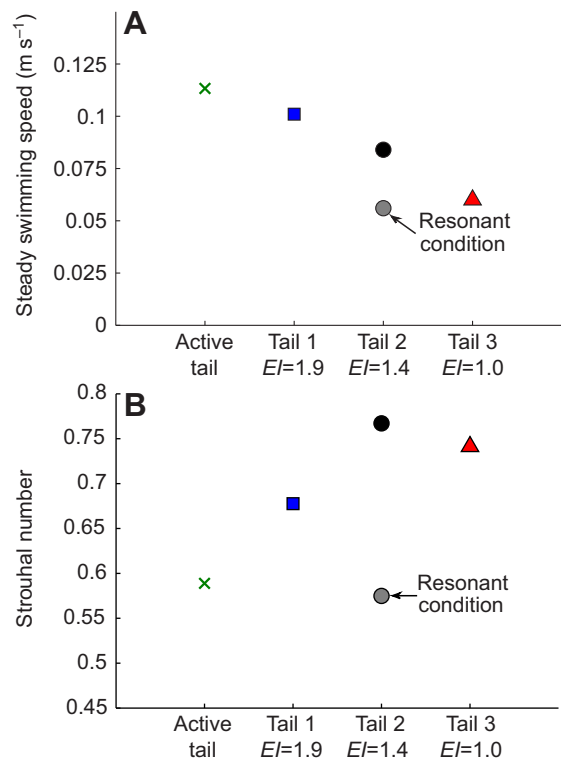


Fig. 10. (A) Steady swimming speeds and (B) Strouhal numbers during steady swimming of the lamprey robot fitted with the active tail and passively flexible tails (tails 1, 2 and 3). At 0.56 Hz, speed decreases as the flexibility increases. However, a decreased in tip-to-tip amplitude of the most flexible tail (tail 3) increases its steady Strouhal number above that of tail 2. In the resonant condition (gray circles), tail 2 oscillates at 0.28 Hz, resulting in a lower steady speed, but the decrease in frequency is larger than the decrease in speed, so the Strouhal number also decreases.

When flapping at the same frequency and amplitude (0.56 Hz and 9.8 cm, corresponding to $St=0.55$), the net force decreases with increasing flexibility, becoming more and more negative (Fig. 11). This general trend agrees with available previous work (e.g. Ferreira de Sousa and Allen, 2011; Masoud and Alexeev, 2010). Tail 1 (the least flexible tail) is the closest to zero momentum flux, meaning that it is closest to the self-propelled state, whereas tail 3 (the most

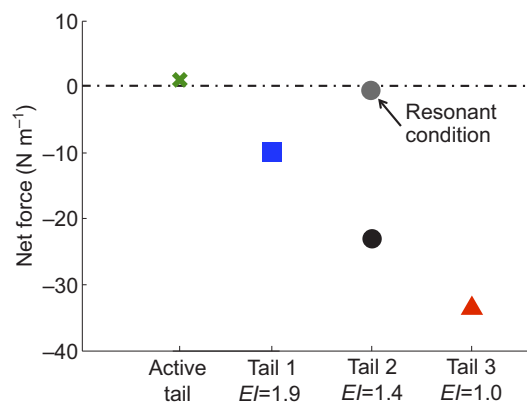


Fig. 11. Net force per unit height of fish body averaged over 20 cycles estimated from the particle image velocimetry data at $St=0.55$. The force is for the entire cycle. Tail 2 is flapping at the resonant frequency.

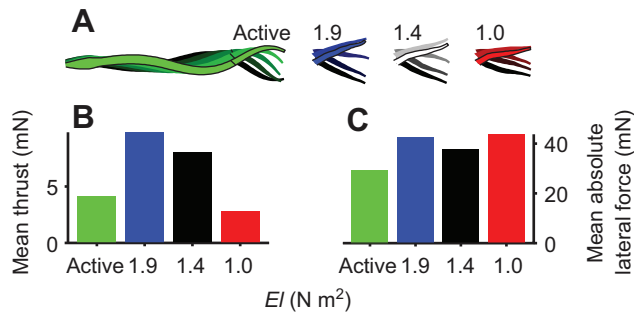


Fig. 12. Thrust and lateral forces for each tail were estimated using its measured kinematics and large-amplitude elongated body theory (Lighthill, 1971). Differences in thrust production seem to be related to a shift in the phase relationship between the tail angle and its side-to-side motion. (A) Kinematics. Colors become brighter to indicate increasing time. Motion of the anterior body (anterior to the lines in the left panel) is identical in all cases. Note that the tail angle at each time step is different for each tail. (B) Mean thrust over a tailbeat cycle has a maximum with the least flexible tail. Positive values indicate force in the forward direction. (C) Mean absolute value of the lateral forces over a tailbeat cycle.

flexible tail) has the most negative flux. In all cases, the overall momentum flux per meter is negative, indicating that there is more drag than thrust being generated. In other words, if the robot was not tethered, it would be expected to move backwards in the tank. At this frequency and amplitude, therefore, the more flexible tails result in a lower self-propelled swimming speed, as shown in Fig. 10.

Given that with any of the flexible tails the robot is no longer swimming under a self-propelled condition, we expect that the wake structures (Fig. 8) will differ from the active tail configuration shown in Fig. 9. For the flexible tails to achieve steady swimming conditions, the incoming flow, U_∞ , would need to be decreased, which would result in an increased Strouhal number. Despite this change, the results presented above show that the main features of the wake are preserved in this deceleration situation.

Thrust and lateral forces were also estimated based on the observed kinematics using the analytical model of Lighthill (Lighthill, 1971) (see our Eqn 5). Fig. 12 shows the kinematics and the mean forces. Increasing passive flexibility tends to decrease thrust. Note that these calculations do not include an estimate of drag, and so are not directly comparable to the net forces shown in Fig. 11. Lateral forces were similar for all of the passive tails. The actively flexing tail, however, produced the lowest thrust. Because its net force was closest to zero (Fig. 11), this suggests that its drag is also lower than the other tails.

As can be observed visually from the flow fields (Fig. 8), the degree of turbulence in the wake increased as tail stiffness decreased. We calculated average turbulence intensity in the wakes of each tail (Fig. 17). For the three stiffnesses, flapping at 0.56 Hz, turbulence intensity increased as tail stiffness decreased. For tail 2, the turbulence intensity decreased when it was flapping at resonance (0.28 Hz), indicating the greater coherence of the wake in the resonant condition. Finally, the actively flexing tail produced the most coherent wake by far, as indicated by the much lower turbulence intensity (Fig. 17).

Corresponding to the decrease in organization of vortices, the momentum flux also becomes less organized in time as tail flexibility increases. The instantaneous net force was estimated using Eqn 4. Fig. 13 shows the instantaneous force per meter

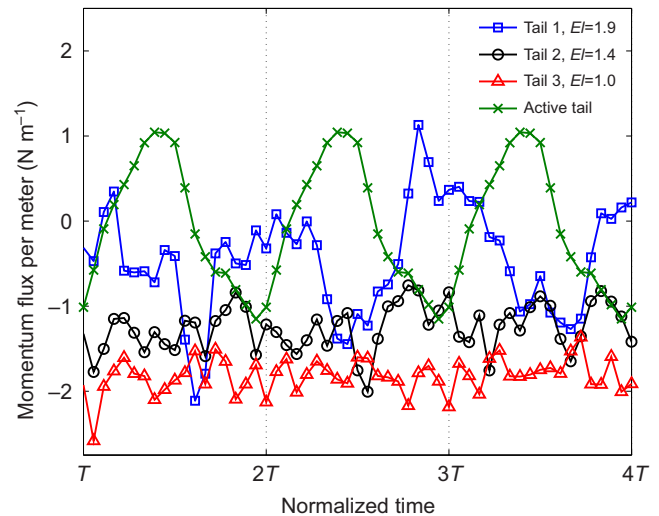


Fig. 13. Instantaneous momentum flux per meter in the half-wake for passive tails 1, 2 and 3 (flapped at 0.56 Hz, $St=0.55$) and the active tail (flapped at 0.56 Hz, $St=0.7$). Time is normalized by the tailbeat period, T . Three cycles of motion are shown.

during three cycles of motion. The mean value follows the same trend as the per cycle total momentum flux per meter presented in Fig. 11. Additionally, the frame-to-frame fluctuations are larger for tail 1 than the two more flexible tails, reflecting the fact that it generates more coherent vortices. In general, there is a maximum and minimum during each cycle of motion for tail 1 (this is also seen in Fig. 14). However, such organization is not as apparent in tails 2 or 3. Although there are peaks and minima present in these signals, they are less regular and distinct. The green line in Fig. 13 is the instantaneous momentum flux for the active tail. It contains a clear peak approximately halfway through the cycle and a minimum just before the cycle's end. There is also a small secondary peak 75% of the way through the cycle. Although tail 1 also has a large peak during the tailbeat cycle, it occurs later in the cycle than the peak for the active tail.

The regularity of the maxima and minima in the instantaneous momentum flux of the robot with tail 1 allows for comparison with the measured velocity fields. In Fig. 14A, five cycles of the instantaneous momentum flux per meter are shown. Frames of minimum and maximum values are indicated by circles on the plot. The corresponding instantaneous vorticity fields (with velocity vectors) are shown in Fig. 14B,C. The schematics above the flow fields indicate the tail position and direction of motion at that time in the cycle. In Fig. 14B, which corresponds to a low point in the instantaneous momentum flux per meter signal, a large structure is seen moving into the control volume in the upper left corner of the frame. This corresponds to a negative momentum flux out of the control volume. The flow field for the point with a high momentum flux (Fig. 14C) shows a large structure moving out of the control volume (right top corner), increasing the net momentum flux out of the control volume.

Resonant frequency

To examine the effects of body resonance on the wake structure, tail 2 was driven at its resonant frequency (0.28 Hz). The Strouhal number, however, was matched to previous experiments ($St=0.55$) by decreasing U_∞ . Fig. 15 shows the vorticity contours computed from the measured velocity field. The overall field is much cleaner

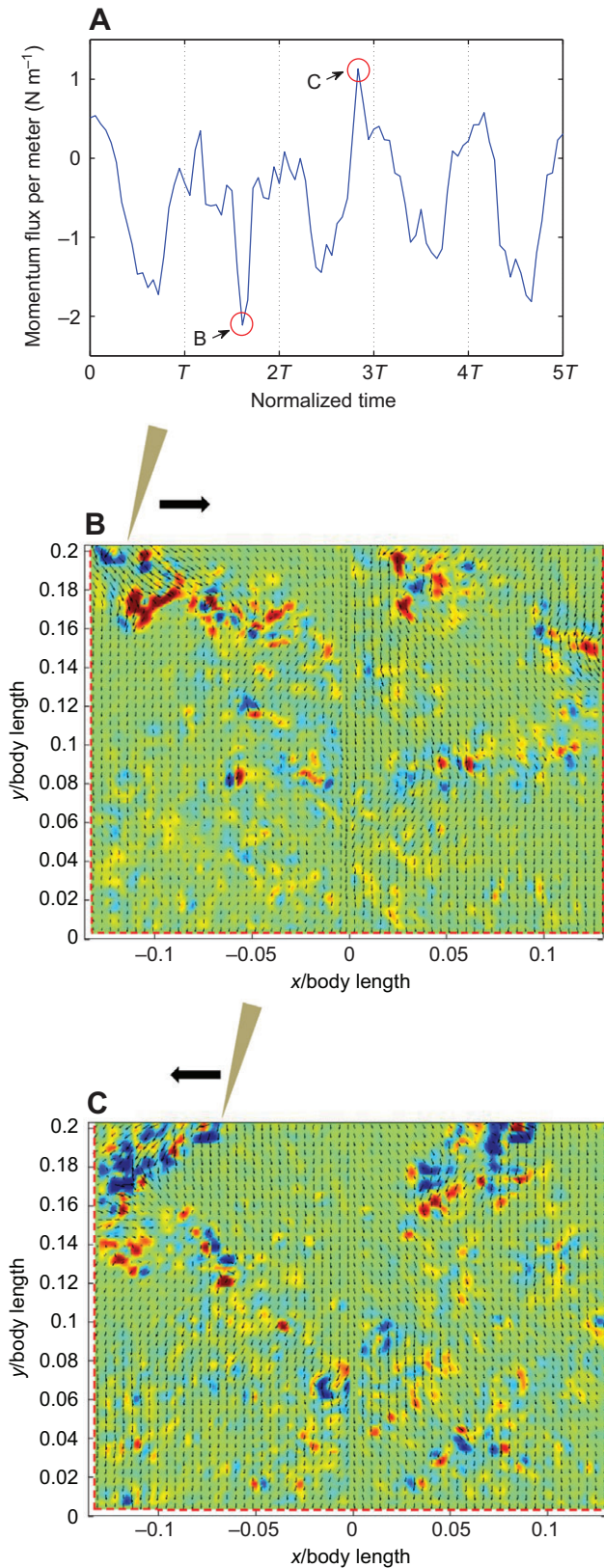


Fig. 14. Comparison of instantaneous momentum flux per meter and the corresponding velocity and vorticity fields. (A) Time course of net momentum flux. Time is normalized by the tailbeat period, T . Instances of low (B) and high momentum flux (C) are shown. Colors indicate vorticity. Flow is from top to bottom. The location and direction of the tail are indicated above each image. The relevant boundaries of the control volume are shown by the red dashed lines.

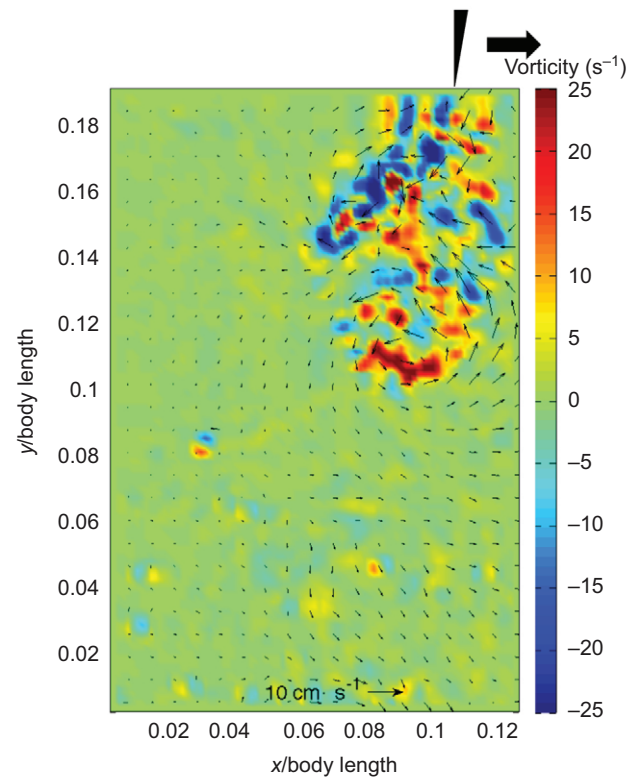


Fig. 15. Flow patterns in the wake of tail 2 flapping at its resonant frequency. Flow is from top to bottom. Instantaneous vorticity contours are plotted in color. Arrows indicate the magnitude and direction of flow with the mean values subtracted. The position of the tail is indicated by the top of the image, and the arrow indicates the direction of tail motion. Compare with the same tail flapping at twice the resonant frequency at the same phase (Fig. 8B).

than that of the same tail flapping at twice the natural frequency (cf. Fig. 8B). There are fewer smaller structures present in the wake away from the main vortices, but there are nevertheless smaller vortices with the same sign that make up the two large oppositely signed vortical structures. Those constitute the 2P structure, which is visible in the upper right portion of the image. The location of those vortices is more predictable from cycle to cycle than they were when the tail was driven above its resonant frequency (0.56 Hz).

As seen in Fig. 11, when the tail is flapped at its resonant frequency, the momentum flux per meter is much higher (there is a 96% increase). Net force is approximately zero, meaning that the robot is nearly propelling itself, much like robot swimming with the active tail. However, when tail 2 is flapped at twice the natural frequency, the momentum flux in this plane drops significantly (if the robot were untethered, it would move backwards in the flow). This increase in capability is also seen in the steady-swimming Strouhal number (Fig. 10B). By flapping at the resonant frequency, the Strouhal number decreases by 25%, moving closer to $St \approx 0.3$, which is generally considered to be peak efficiency for undulatory swimmers (Triantafyllou et al., 1993).

Fig. 16 shows a comparison of the instantaneous moment flux for tail 2 at these two frequencies. In addition to an increased mean value, the fluctuations are larger for flapping at resonant frequency. The curve at the resonant frequency has more distinct maxima and minima than the curve at the higher frequency, but the peaks are not as distinct as with tail 1 (see Fig. 13).

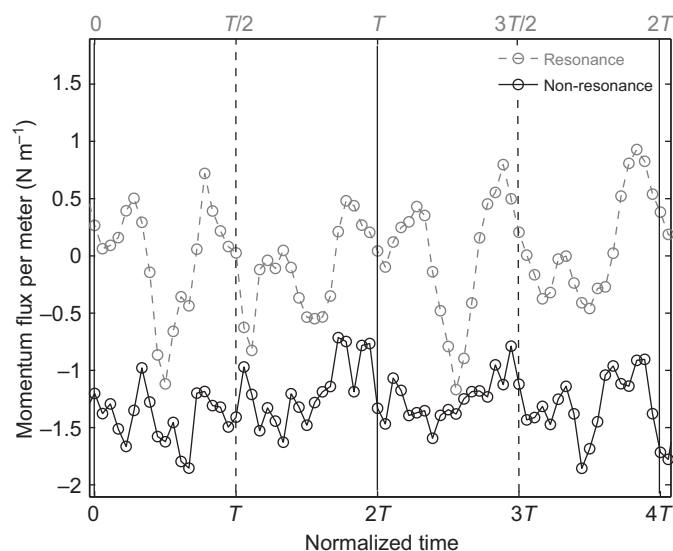


Fig. 16. Instantaneous momentum flux per meter for tail 2 flapped at 0.56 Hz (non-resonance) and 0.28 Hz (resonance). Time is normalized by the tailbeat period, T . Four cycles of motion are shown at 0.56 Hz, and two cycles are shown at 0.28 Hz.

DISCUSSION

In summary, a robotic anguilliform swimmer with a passively flexible tail produces qualitatively the same wake structure as the same robot with an actively flexing tail (Hultmark et al., 2007) and the same as swimming eels (Tytell and Lauder, 2004). Although the wake is qualitatively the same, it is less coherent than those of eels or the robot with the active tail. The wakes of the flexible tails have a higher turbulence intensity than that of the active tail (see Fig. 17). Eels have very flexible bodies (Aleyev, 1977), but they actively control body flexion (Gillis, 1998) and most likely control fin ray motion, like other fishes (Flammang and Lauder, 2008).

Wake coherence

The disorganized wake structures may be a consequence of vortex-induced vibration in the passive tails, particularly along the edges that correspond to the location of the caudal, dorsal and anal fins. This vibration was less than 2 cm in all cases, but was particularly noticeable for the most flexible tail, which may account for its especially disorganized wake (Fig. 8C). The high flexibility of fish bodies suggests that they also have the potential to develop such vibrations. However, the coherence of fish wakes (Lauder and Tytell, 2006) suggests that they may be able to damp out vibrations. It is also likely that fish swim 'in tune' with their own natural frequencies, helping them to produce coherent wakes. In walking animals, muscle is used to damp out such high-frequency oscillations (Wakeling et al., 2003; Wilson et al., 2001), and although such an effect has not been observed directly in fishes, perhaps fin ray muscles could serve to filter out vortex-induced vibrations.

Additionally, the fact that the robot was, in essence, being towed (i.e. the net force was negative), may be another cause of the disorganized wake structure. The speed of the incoming flow can cause instabilities in the boundary layer along the body (Shen et al., 2003). This can decrease the cohesiveness of the vortices as they are shed into the wake. Therefore, more small structures – both in the main vortex pairs and away from these features – are likely to be present in the wake. This is seen when we compare Fig. 8B

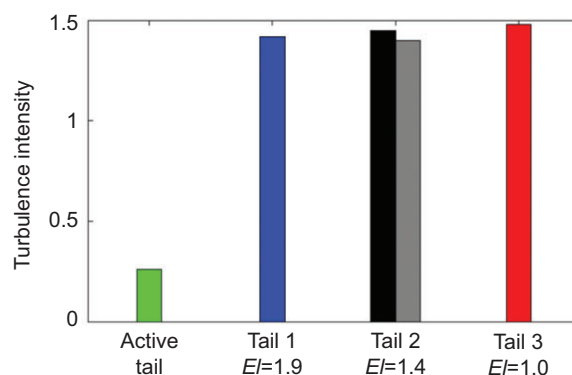


Fig. 17. Mean turbulence intensity for the active tail and three passive tails [data for tail 2 are given for twice its resonance frequency (black bar) and at resonance (gray bar)] averaged over one cycle of motion.

with the resonant wake of tail 2. Both the resonant and non-resonant conditions had $St=0.55$, but the frequency was lower in the resonant case, so U_∞ was also lower. In the resonant case, we see far fewer small vortex structures away from the main vortex pair (Fig. 15) and a slight decrease in turbulence intensity (Fig. 17). However, structures are still present within that pair, suggesting that passive flexibility (as described above) also plays an important role in decreasing wake coherence.

Data from fishes suggest that they produce relatively well-organized wakes (Lauder and Tytell, 2006), but a disorganized wake may sometimes be helpful. The wakes of swimming fishes can persist for long periods of time (Hanke and Bleckmann, 2004), and predators are able to follow the residual flow patterns (Schulte-Pelkum et al., 2007). Disorganized wakes, such as those produced by the passively flexible tails, tend to decay more rapidly than well-organized wakes (like that of the active tail), leaving a smaller signature for predators to detect. In particular, the wake behind tail 2, flapping at its resonant frequency, showed very little structure in the far wake ($y < 0.1$ in Fig. 15), but nevertheless produced enough thrust to propel itself (Figs 13, 16). Fishes differ in the amount of time their wakes persist (Hanke and Bleckmann, 2004); perhaps they can control this duration by changing the coherence of the wake.

Thrust production

Nevertheless, our results suggests that, when other conditions are the same, increasing the passive flexibility of an anguilliform propulsor results in an increasingly large negative (i.e. drag-like) net force, either by decreasing the forward thrust production or increasing the drag. We find that net momentum flux is more negative for increasingly flexible tails (Figs 11, 13).

A simple model (Eqn 5) based on Lighthill's elongated body theory (Lighthill, 1971) suggests that a decrease in thrust (Fig. 12) may be the most important factor, rather than an increase in drag. Elongated body theory suggests that thrust is maximized when tail angle is relatively large when tail speed is high. For tail 1 ($EI=1.9 \text{ Nm}^2$), tail angles are close to 45 deg when tail speed is high, but the tail angles are smaller in general for the more flexible tail ($EI=1.0 \text{ Nm}^2$; Fig. 12A), and are at a less-optimal phase relative to the tail motion. Thus, the changes in kinematics due to increasing flexibility may account for the decrease in thrust and the more negative momentum flux (Fig. 11). Interestingly,

the active tail also has a low mean thrust (Fig. 12B) but a net force close to zero. Together, these results suggest that the robot with the active tail may have a lower drag than when it has a passive tail.

Our results are generally consistent with previous computational studies. Tytell et al. (Tytell et al., 2010) developed a model of fluid–structure interaction for a swimming lamprey and found that swimming speed increased with increasing stiffness (similar to our Fig. 10), except at the very highest stiffness. Similarly, Ferreira de Sousa and Allen (Ferreira de Sousa and Allen, 2011) simulated a flexible rod and found, in general, that thrust increased with increasing stiffness, except at the very lowest stiffness. Both of these previous models cannot be compared directly with our results because they kept the driving force constant, resulting in different tailbeat amplitudes and thus different Strouhal numbers for models with different stiffness, whereas we altered the driving amplitude in order to match Strouhal number for the different values of stiffness. Nevertheless, the general patterns are consistent. Our observation of increased thrust at resonance (Fig. 11) is also similar to the simulation results of Masoud and Alexeev (Masoud and Alexeev, 2010), who found a dramatic increase in lift force for a flapping wing at resonance.

Fishes also actively control tail bending. The lamprey has muscle present all the way to the tip of its tail and, like other fishes, has muscles that control fin motion. The fin musculature is known to be active during pharmacologically stimulated fictive swimming (Mentel et al., 2008), but it is not known how the fins are activated during natural swimming. In bluegill sunfish, the caudal fin musculature is active even at the slowest swimming speeds when the fish does not use the caudal fin for propulsion (Flammang and Lauder, 2008). Thus, fishes most likely actively flex their tails even at slow speeds. However, the fin muscles are quite small and the forces they can produce are also small. Thus, fluid pressure on the fin is likely to have a strong effect on fin motion.

In this study and a previous one (Hultmark et al., 2007), we have investigated two extremes: completely active motion, in which internal forces (i.e. the motors) completely dominate external fluid forces (Hultmark et al., 2007), and the completely passive motions described here, in which the tail bending is entirely determined by the fluid forces. The motion of fish tails probably lies somewhere between these two extremes; we postulate that they are closer to the passive extreme investigated here than the completely active extreme from Hultmark et al. (Hultmark et al., 2007).

Conclusions

Increasing the flexibility of the tail of an anguilliform swimmer decreases the coherence of the vortices in the wake. However, even with a very flexible tail, a 2P structure is still visible. The wake of the most flexible tail also breaks down faster. The net force is lower for more flexible tails, most likely because of decreased thrust production. However, by flapping the tail at its resonant frequency, the net force becomes less negative, approaching the self-propelled state, and the wake regains much of its coherence.

FUNDING

Financial support for this project was provided by the National Institutes of Health [grant R01 NS054271 to A.H.C.]. Deposited in PMC for release after 12 months.

REFERENCES

- Aleyev, Y. (1977). *Nekton*. The Hague: W. Junk.
- Borazjani, I. and Sotiropoulos, F. (2008). Numerical investigation of the hydrodynamics of anguilliform swimming in the transitional and inertial flow regimes. *J. Exp. Biol.* **212**, 576–592.
- Buchholz, J. H. J. (2006). *The Flowfield and Performance of a Low Aspect Ratio Unsteady Propulsor*. PhD thesis, Princeton University, Princeton, NJ, USA.
- Den Hartog, J. (1961). *Strength in Materials*. New York: Dover Publications.
- DuBois, A. B. and Ogilvy, C. S. (1978). Forces on the tail surface of swimming fish: thrust, drag and acceleration in bluefish (*Pomatomus saltatrix*). *J. Exp. Biol.* **77**, 225–241.
- Ferreira de Sousa, P. J. S. A. and Allen, J. J. (2011). Thrust efficiency of harmonically oscillating flexible flat plates. *J. Fluid Mech.* **674**, 43–66.
- Flammang, B. E. and Lauder, G. V. (2008). Speed-dependent intrinsic caudal fin muscle recruitment during steady swimming in bluegill sunfish, *Lepomis macrochirus*. *J. Exp. Biol.* **211**, 587–598.
- Gillis, G. B. (1998). Neuromuscular control of anguilliform locomotion: patterns of red and white muscle activity during swimming in the American eel *Anguilla rostrata*. *J. Exp. Biol.* **201**, 3245–3256.
- Gray, J. (1933). Studies in animal locomotion. I. The movement of the fish with special reference to the eel. *J. Exp. Biol.* **10**, 88–103.
- Hanke, W. and Bleckmann, H. (2004). The hydrodynamic trails of *Lepomis gibbosus* (Centrarchidae), *Colomesus psittacus* (Tetraodontidae) and *Thysochromis ansorgii* (Cichlidae) investigated with scanning particle image velocimetry. *J. Exp. Biol.* **207**, 1585–1596.
- Hultmark, M., Leftwich, M. C. and Smits, A. J. (2007). Flowfield measurements in the wake of a robotic lamprey. *Exp. Fluids* **234**, 683–690.
- Jordan, C. E. (1996). Coupling internal and external mechanics to predict swimming behavior: a general approach. *Am. Zool.* **36**, 710–722.
- Lauder, G. V. and Tytell, E. D. (2006). Hydrodynamics of undulatory propulsion. In *Fish Biomechanics* (ed. R. E. Shadwick and G. V. Lauder), pp. 425–468. San Diego, CA: Academic Press.
- Leftwich, M. C. and Smits, A. J. (2011). Thrust production by a mechanical swimming lamprey. *Exp. Fluids* **50**, 1349–1355.
- Lighthill, M. J. (1970). Aquatic animal propulsion of high hydromechanical efficiency. *J. Fluid Mech.* **44**, 265–301.
- Lighthill, M. J. (1971). Large-amplitude elongated-body theory of fish locomotion. *Proc. R. Soc. Lond. B* **179**, 125–138.
- Long, J. H. (1998). Muscles, elastic energy, and the dynamics of body stiffness in swimming eels. *Am. Zool.* **38**, 771–792.
- Masoud, H. and Alexeev, A. (2010). Resonance of flexible flapping wings at low Reynolds number. *Phys. Rev. E* **81**, 056304.
- McHenry, M. J., Pell, C. A. and Long, J. H. (1995). Mechanical control of swimming speed: stiffness and axial wave for in undulating fish models. *J. Exp. Biol.* **198**, 2293–2305.
- Mentel, T., Cangiano, L., Grillner, S. and Buschges, A. (2008). Neuronal substrates for state-dependent changes in coordination between motoneuron pools during fictive locomotion in the lamprey spinal cord. *J. Neurosci.* **28**, 868–879.
- Müller, U. K., Smit, J., Stamhuis, E. J. and Videler, J. J. (2001). How the body contributes to the wake in undulatory fish swimming: flow fields of a swimming eel (*Anguilla anguilla*). *J. Exp. Biol.* **204**, 2751–2762.
- Nauen, J. C. and Lauder, G. V. (2002). Hydrodynamics of caudal fin locomotion by chub mackerel, *Scomber japonicus* (Scombridae). *J. Exp. Biol.* **205**, 1709–1724.
- Schulte-Pelkum, N., Wieskotten, S., Hanke, W., Dehnhardt, G. and Mauck, B. (2007). Tracking of biogenic hydrodynamic trails in harbour seals (*Phoca vitulina*). *J. Exp. Biol.* **210**, 781–787.
- Shen, L., Zhang, X., Yue, D. K. P. and Triantafyllou, M. S. (2003). Turbulent flow over a flexible wall undergoing a streamwise travelling wave motion. *J. Fluid Mech.* **484**, 197–221.
- Shoole, K. and Zhu, Q. (2009). Fluidstructure interactions of skeleton-reinforced fins: performance analysis of a paired fin in lift-based propulsion. *J. Exp. Biol.* **212**, 2679–2690.
- Smits, A. J. (2000). *A Physical Introduction to Fluid Mechanics*. New York: John Wiley.
- Tangorra, J. L., Lauder, G. V., Hunter, I. W., Mittal, R., Madden, P. G. A. and Bozkurtas, M. (2010). The effect of fin ray flexural rigidity on the propulsive forces generated by a biorobotic fish pectoral fin. *J. Exp. Biol.* **213**, 4043–4054.
- Triantafyllou, G. S., Triantafyllou, M. S. and Grosenbaugh, M. A. (1993). Optimal thrust development in oscillating foils with application to fish propulsion. *J. Fluid Struct.* **7**, 205–224.
- Tytell, E. D. and Lauder, G. V. (2004). The hydrodynamics and eel swimming. I. Wake structure. *J. Exp. Biol.* **207**, 1825–1841.
- Tytell, E. D., Hsu, C. Y., Williams, T. L., Cohen, A. H. and Fauci, L. J. (2010). Interactions between internal forces, body stiffness, and fluid environment in a neuromechanical model of lamprey swimming. *Proc. Natl. Acad. Sci. USA* **107**, 19832–19837.
- Wakeling, J. M., Liphardt, A. M. and Nigg, B. M. (2003). Muscle activity reduces soft-tissue resonance at heel-strike during walking. *J. Biomech.* **36**, 1761–1769.
- Williamson, C. H. K. and Roshko, A. (1988). Vortex formation in the wake of an oscillating cylinder. *J. Fluid Struct.* **2**, 355–381.
- Wilson, A. M., McGuigan, M. P., Su, A. and van den Bogert, A. J. (2001). Horses damp the spring in their step. *Nature* **414**, 895–899.
- Zhu, Q. and Shoole, K. (2008). Propulsion performance of a skeleton-strengthened fin. *J. Exp. Biol.* **211**, 2087–2100.